Invited Paper

Asymmetric rotational axis reconstruction of grating-based X-ray phase contrast tomography of the human cerebellum

Georg Schulz[a], Timm Weitkamp[b,c], Irene Zanette[b,d], Franz Pfeiffer[d], Magdalena Müller-Gerbl[e], Christian David[f], and Bert Müller[a]

[a]Biomaterials Science Center, University of Basel, Basel, Switzerland;
[b]European Synchrotron Radiation Facility (ESRF), Grenoble, France;
[c]Synchrotron SOLEIL, Gif-sur-Yvette, France;
[d]Biomedical Physics, Technische Universität München, Garching, Germany;
[e]Institute of Anatomy, University of Basel, Basel, Switzerland;
[f]Laboratory for Micro- and Nanotechnology, Paul Scherrer Institut, Villigen, Switzerland

ABSTRACT

The brain has an outstanding functional importance in the human organism. Therefore, there is a strong need for three-dimensional brain imaging modalities. Magnetic resonance imaging provides deep insights but its spatial resolution is insufficient to study the structure on the cellular level. X-ray absorption microtomography yields the necessary spatial resolution, but shows only marginal contrast between the different types of brain tissue. Alternatively, differential X-ray phase contrast obtained with grating interferometry, which is known for much better differentiations between soft tissues can be used for the visualization of the human brain. As important structures of the human brain such as the human thalamus have dimensions of several centimeters, a large field of view is required. In the present communication, we report an evaluation of grating-based X-ray phase contrast microtomography in the off-axis modus which allows to expand the field of view up to a factor of two but may reduce the image quality. We demonstrate that tomograms with comparable contrast-to-noise values, about 10%, and 50% inferior spatial resolution can be generated with off-axis measurements. As one can reduce the effective pixel size up to a factor of two, the choice of an asymmetrical rotation axis can give rise to an improvement of the spatial resolution by 20%.

Keywords: spatial and density resolution, grating interferometer, synchrotron radiation-based microtomography, half acquisition, asymmetric rotation axis reconstruction, brain tissue

1. INTRODUCTION

For the visualization of the human brain on the cellular level, microimaging techniques with large field of views (FOV) are of high interest. Depending on which structure is investigated sometimes FOVs of several centimeters are required. Using absorption contrast X-ray tomography, the effective FOV can be increased by means of an off-axis scan where the rotation axis is shifted from its usual position near the center of the image to a position near the left or right edge of the field and a 360° scan is performed [1, 2], a technique sometimes referred to as "half-object acquisition" or simply "half acquisition" [3]. Unfortunately, absorption contrast microtomography (μCT) only shows marginal contrast for soft tissues, in particular for brain tissues. Magnetic resonance imaging (MRI) which is well known as a non-destructive three-dimensional (3D) imaging technique with high contrast between white and gray matter. Unfortunately, the limited spatial resolution of around two magnitudes larger than that of microtomography inhibits investigation on the cellular level.

A better contrast compared to absorption-based studies can be obtained by synchrotron radiation-based phase-contrast μCT (PC-μCT) [4, 5] which was recently applied to human brain [6]. X-ray phase-contrast is based on the phase shifts of X-ray waves penetrating the specimen. Different PC-μCT methods based on crystal interferometry [7, 8], propagation-based contrast [9, 10] or analyzer-based imaging (ABI) [11, 12] are available

Further author information: (Send correspondence to G.S.)
E-mail: georg.schulz@unibas.ch, Telephone: +41 61 265 9127, Fax: +41 61 265 9699

Developments in X-Ray Tomography VIII, edited by Stuart R. Stock,
Proc. of SPIE Vol. 8506, 850604 · © 2012 SPIE · CCC code: 0277-786/12/$18
doi: 10.1117/12.928487

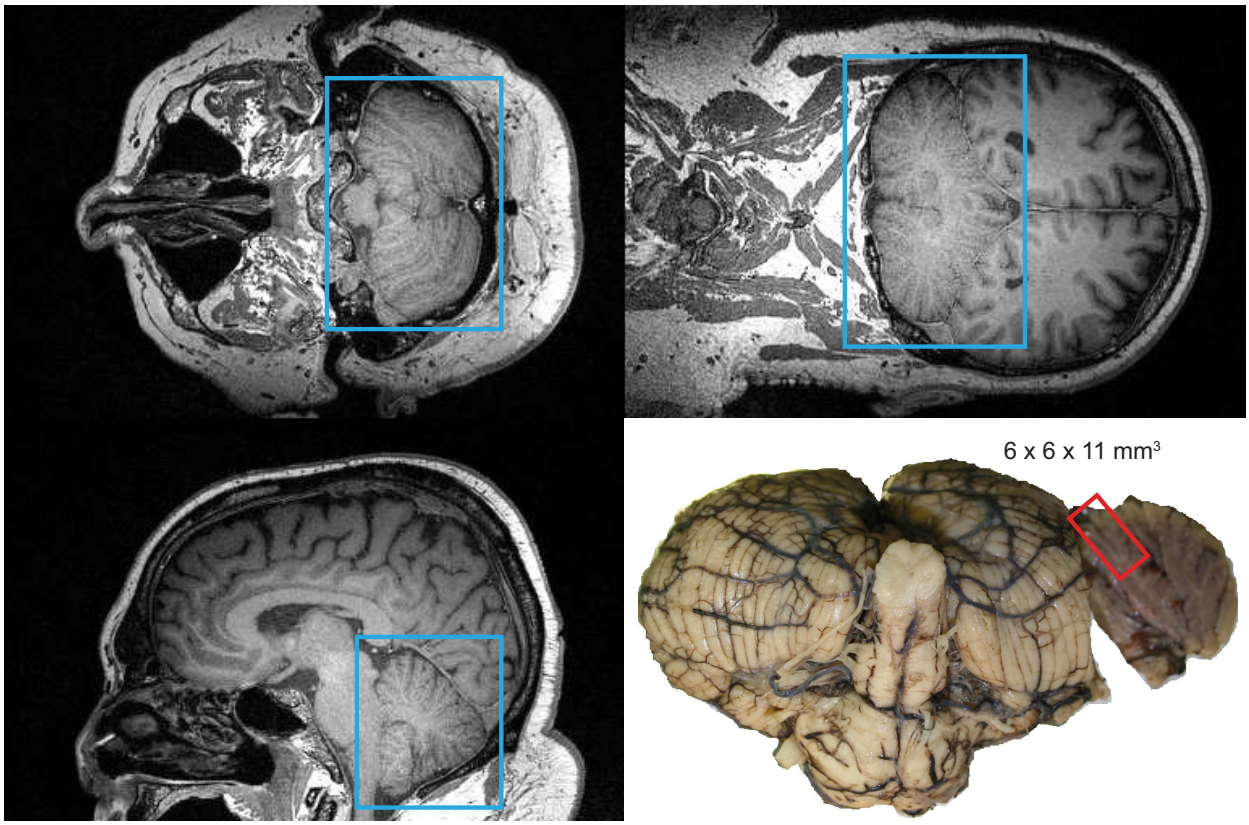

Figure 1. Orthogonal magnetic resonance imaging slices illustrate the position of the cerebellum within the head. The photograph shows the position of the specimen within the extracted cerebellum.

today. Because of its high sensitivity, the more recently developed grating interferometry [13–15] (also known as Talbot interferometry) seems to be a better choice for identifying structures with small differences in electron density as is the case in soft tissues [16], especially in brain tissues [6, 17–19].

As we are interested in large FOVs, the question arises if it is possible to image large human brain specimens using an off-axis scan modus. So far images of the human thalamus [20] and human urethra [21] were acquired using asymmetric rotation axis scans. The aim of this manuscript is to directly compare a full-view scan (i.e., with the axis near the center of the image and a field of view covering the full object width) with an off-axis scan and to quantify the differences.

2. MATERIALS AND METHODS

2.1 Specimen preparation

After the extraction of the brain from the donated body of a 68-year-old male at the Institute of Anatomy (University of Basel, Switzerland), within 48 h after death the whole brain was transferred into a container filled with 10% formalin solution for fixation. The procedures were conducted in accordance with the Declaration of Helsinki and according to the ethical guidelines of the Canton of Basel, Switzerland. The extraction of the cerebellum block ($6 \times 6 \times 11$ mm^3) was carried out at the University Hospital Zurich, Switzerland, after approximately three months of fixation. During the measurements the specimen was placed in an Eppendorf container filled with 4% formalin solution for PC-μCT. The position of the cerebellum within the brain can be recognized by the orthogonal MR slices in Fig. 1. The photograph of Fig. 1 shows the position of the extracted specimen within the cerebellum. It should be noted that the brain tissue exhibits expansion after removal from the cranium and shrinkage after formalin fixation [22].

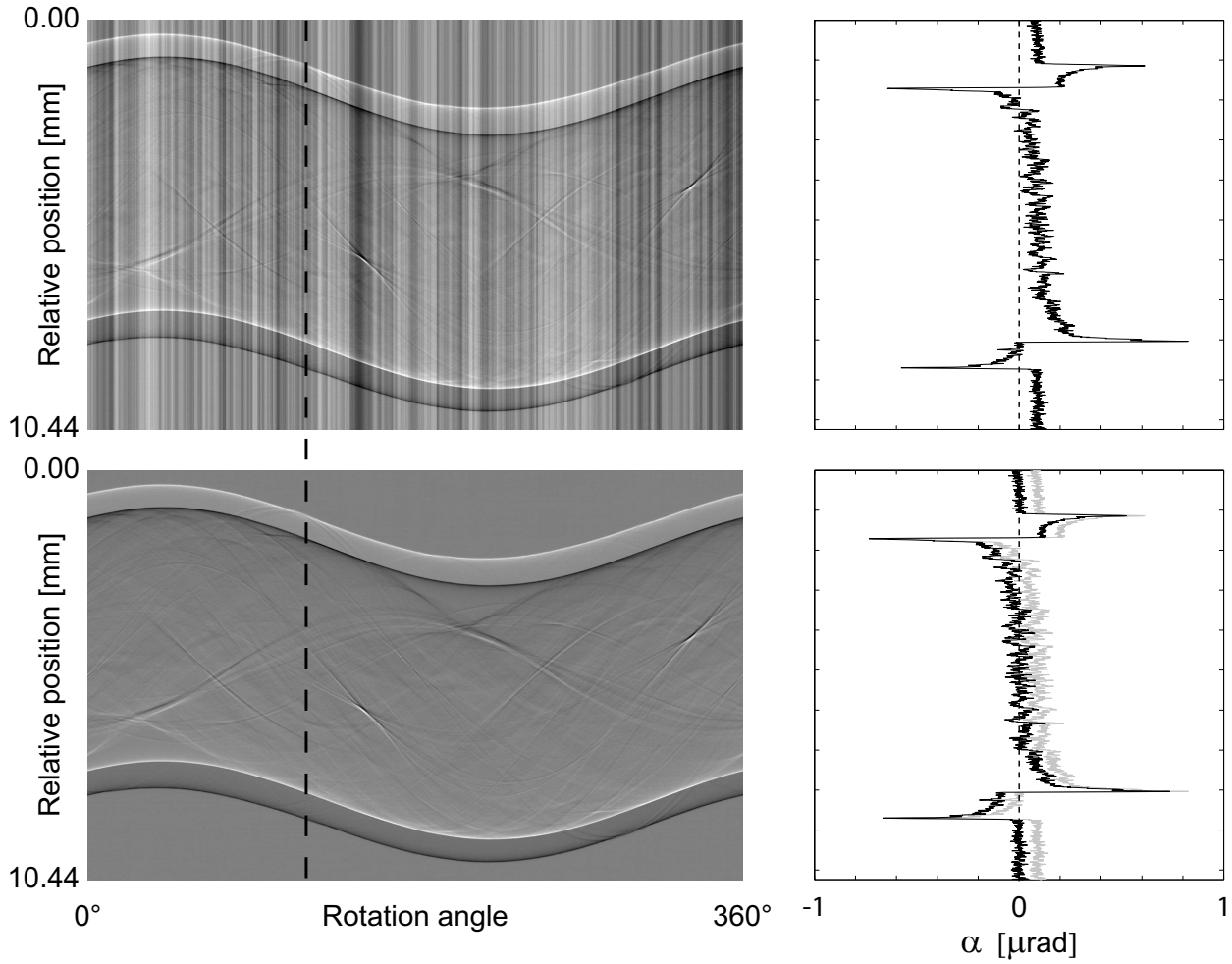

Figure 2. The selected sinogram of the full-view scan (top left) and the line plot through it illustrate artifacts arising from inaccuracies of the grating postions which can be corrected by the linewise subtraction of the mean values (bottom).

2.2 Grating-based phase contrast

X-ray phase contrast microtomography provides information about the three-dimensional distribution of the real part of the decrement of the refractive index of an object $\delta(x, y, z)$. For X-ray energies far away from the absorption edges, δ relates to the electron density distribution $\rho(x, y, z)$ via equation

$$\delta(x, y, z) = \frac{r_e \lambda^2}{2\pi} \rho(x, y, z), \tag{1}$$

containing the classical electron radius r_e and the X-rays wavelength λ. A grating interferometer is not sensitive to the phase shift $\Phi(y, z)$ itself but to the X-ray deflection angle $\alpha(y, z)$ which is proportional to the first derivative of the phase shift and is related to $\delta(x, y, z)$ by

$$\alpha(y, z) = \frac{\lambda}{2\pi} \frac{\partial \Phi(y, z)}{\partial y} = \int_{-\infty}^{\infty} \frac{\partial \delta(x, y, z)}{\partial y} dx. \tag{2}$$

A detailed description of grating interferometry, in particular the phase-stepping method, can be found in literature [14, 15].

The phase contrast experiments were carried out at the beamline ID19 (ESRF, Grenoble, France). Using the interferometer installed there [23] X-rays were taken from a U32 undulator with a gap set to 15.15 mm.

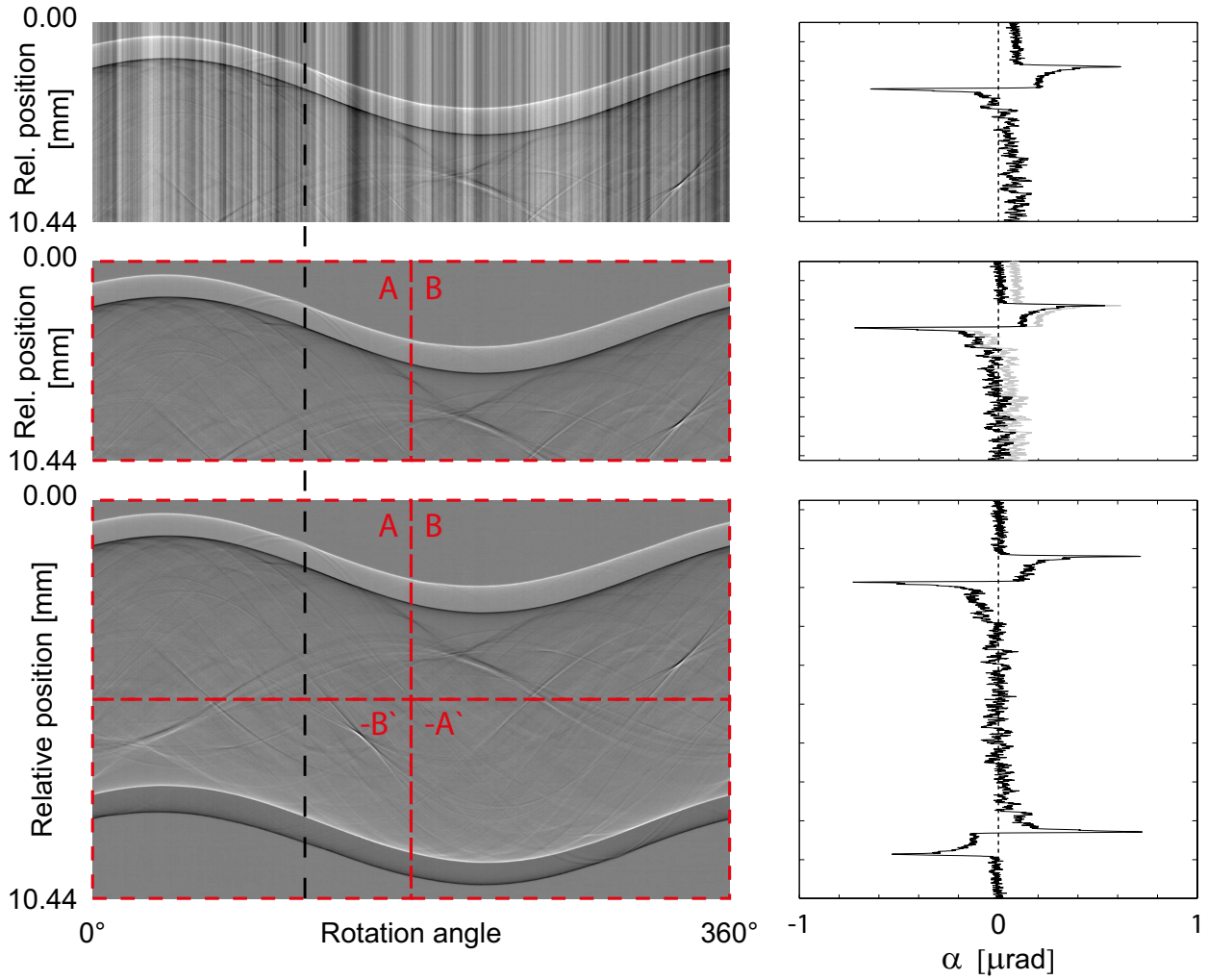

Figure 3. The correction of the off-axis sinogram cannot be performed as represented in Fig. 2. Here the line plots can be corrected by subtracting the mean value of the background signal (middle). For the combination of the sinogram the blocks A and B were multiplied by (-1) and reflected horizontally. After that they were placed as illustrated in the sinogram on the bottom.

Using a double-crystal Si(111)-monochromator in Bragg geometry the photon energy of 23 keV was selected. The imaging of the entire specimen required two scans to obtain a field of view 11 mm high and 6 mm wide. The beam-splitter grating g_1 (Paul Scherrer Institut, Villigen, Switzerland) had a periodicity of $p_1 = 4.785$ μm and a Si structure height of 29 μm, which corresponds to a phase shift of π for 23-keV X rays. The analyzer grating g_2 (Karlsruhe Institute of Technology, Eggenstein-Leopoldshafen, Germany) consisted of lines of gold with a periodicity of $p_2 = 2.400$ μm and a Au structure height of 50 μm. This resulted in an intensity transmission of only about 6×10^{-3} through the lines of the analyzer grating, corresponding to a contrast of 100%. With a distance between source and interferometer of 150 m and a distance between the gratings of $d = 479.4$ mm, corresponding to the 9^{th} Talbot order, the ratio of the grating periods p_2/p_1 was matched to the beam divergence [24]. During the measurements, the Eppendorf container was placed in a water tank with parallel polymethylmethacrylate plates in order to minimize artefacts due to X-ray phase curvature induced by a conical container-air interface. The water tank was located 10 cm upstream of the beam-splitter grating. The detector was a lens-coupled scintillator and charge-coupled device (CCD) system using a FreLoN 2K (Fast-Readout, Low-Noise, ESRF Grenoble, France) CCD with 2048 $\times$ 2048 pixels and an effective pixel size of 5.1 μm. It was placed approximately 3 cm

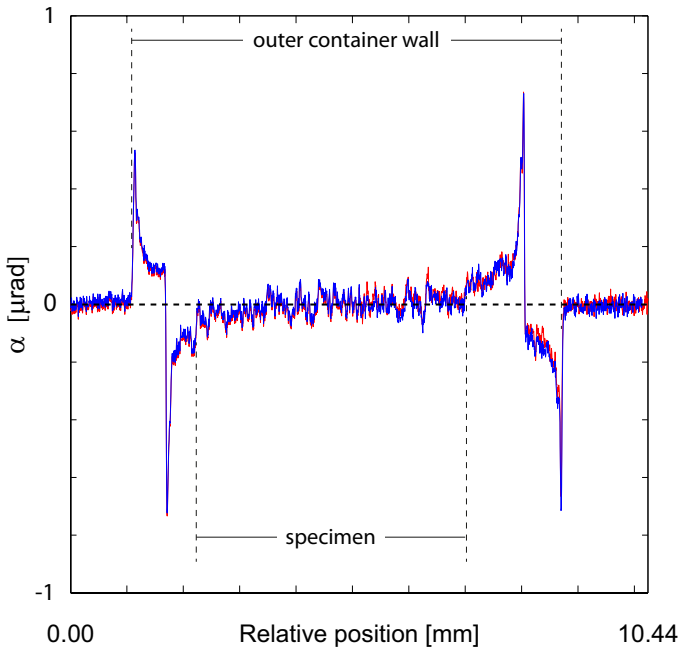

Figure 4. Line plots through the full-view sinogram (red) in comparison to the off-axis sinogram (blue). Besides small differences of the deflection values α, the line plots show an equivalent distribution, in particular the positions of the peaks are unchanged.

downstream of the analyzer grating. Projection radiographs were taken in 1501 steps over a range of 360°. At each projection angle, four phase-stepping images with an exposure time of 1 s each were taken over one period of the interference pattern.

2.3 Data treatment

The first step after the acquisition of the data was the processing of the projections and the generation of the sinograms. The differential phase-contrast sinograms contain artifacts in the form of an offset value added to each projection. These offsets vary from projection to projection. They can be corrected simply by a line by line subtraction of the mean values (see Fig. 2).

The generation of the off-axis sinograms was arranged by taking half projections. After producing the off-axis sinograms (Fig. 3 top left) they can not be corrected by the linewise subtraction of the mean values as the failure of information on the opposite side of the histogram would lead to wrong offsets of the line plots. However the correction can be arranged by subtracting the mean value of the background signal (in this case a mean value of 50 pixels of the water values), which theoretically should be zero (see Fig. 3 center). After the correction the sinograms were assembled by multiplying the parts A and B of the half sinogram with (-1), reflecting them horizontally and placing them on the positions shown in Fig. 3 bottom left.

In order to obtain comparable scan conditions (in particular comparable angular sampling and photon statistics) every other line of the full-view scan sinograms were deleted. After the generation of the sinograms the reconstruction was carried out using a modified filter kernel (Hilbert transform) in combination with standard back-projection algorithm [25–27]. All the data treatment steps were performed using Matlab 7.8 (MathWorks, Natick, USA).

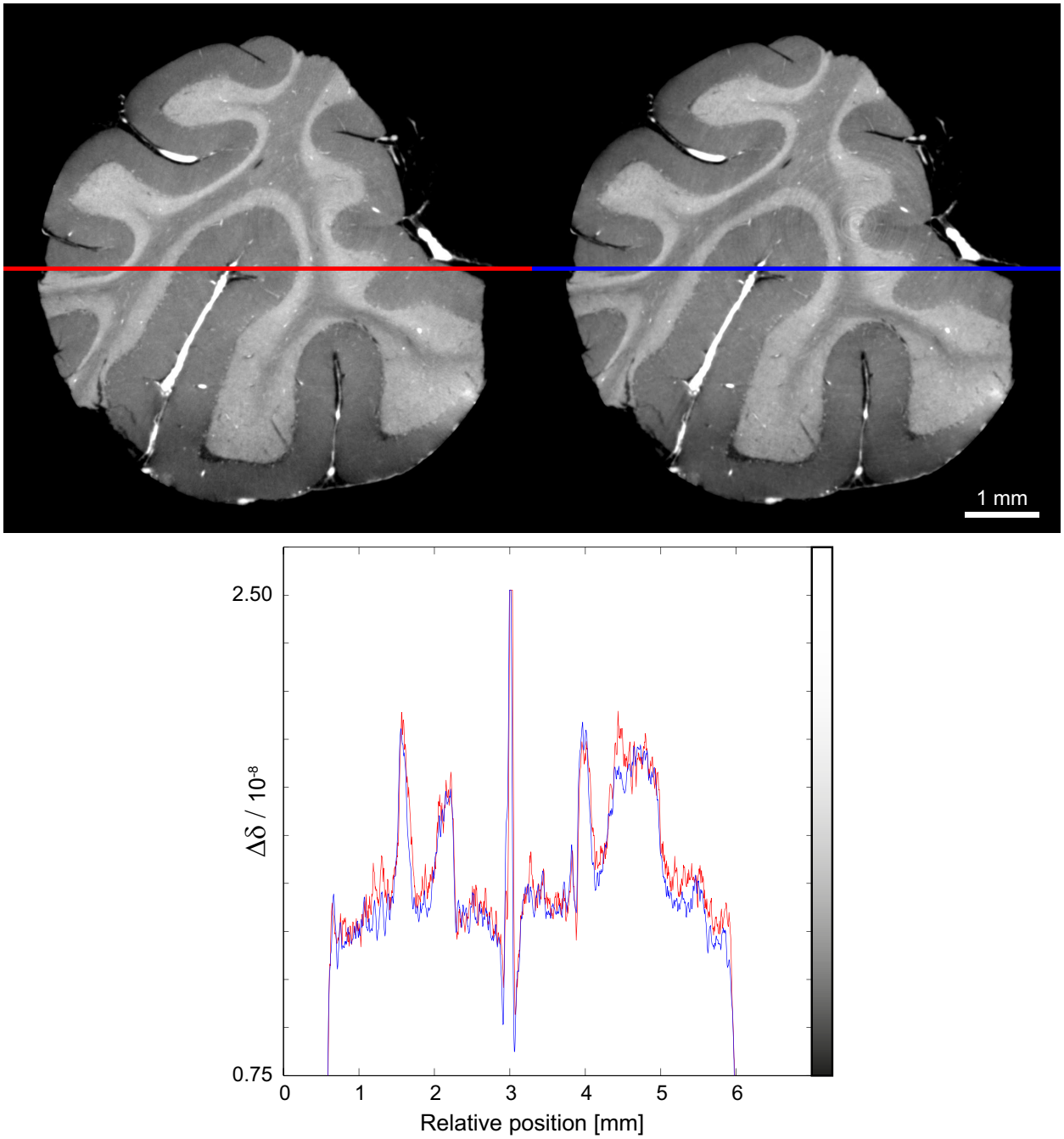

Figure 5. One selected slice of the cerebellum block reconstructed using the full-view (left) and the off-axis (right) data sets. Line plots through the two slices (bottom) illustrate the differences of the differently reconstructed data sets.

3. RESULTS AND DISCUSSION

3.1 Creation of sinograms

Fig. 4 shows a comparison of, a) the line plots of the full-view scan (red), corrected by the mean value of the whole line and, b) the line plot of the off-axis scan (blue), corrected by the mean value of the background signal. The the sinogram was assembled by the two blocks A and B of the half sinogram (cp. Fig. 3). The positions of

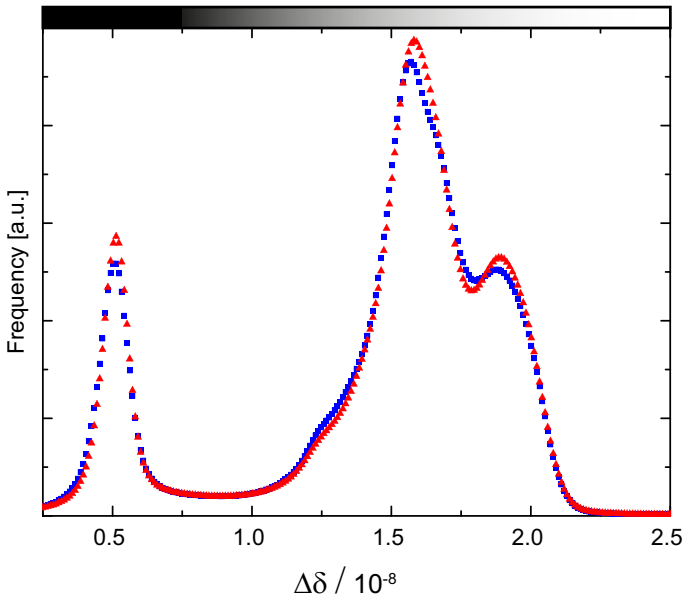

Figure 6. Histograms of the 3D data sets reconstructed using the full-view sinograms (red triangles) and the off-axis sinograms (blue squares). Only slight changes of the positions and widths can be recognized.

the peaks within the line plots are well reproduced whereas some slight changes in the deflection angle α can be detected.

3.2 Morphology of the human cerebellum

The morphology of the human cerebellum can be properly visualized by the reconstructed slices in Fig. 5. On the left hand side one selected reconstructed slice of the full-view data set and on the right hand side a slice of the off-axis data set are shown. Both slices allow a clear differentiation between four structures. The inner

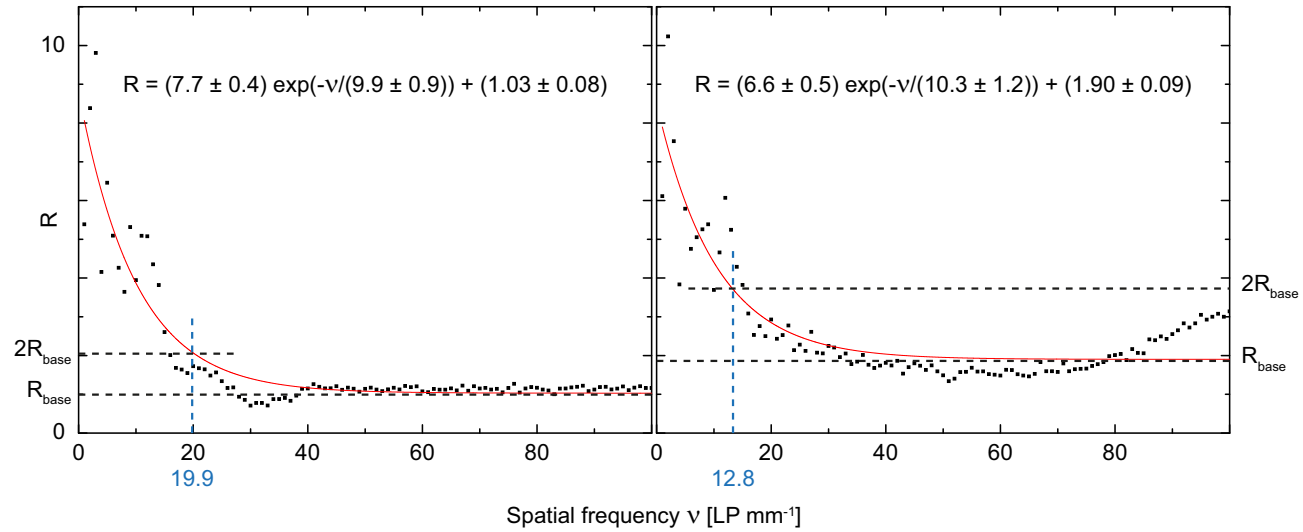

Figure 7. The calculation of the spatial resolution by means of Fourier analysis of the data sets. There, the ratio R between $\mathrm{rSP}_{\mathrm{struc}}$ of a tomogram ROI with a fine structure and $\mathrm{rSP}_{\mathrm{back}}$ of a tomogram ROI with background (water) was plotted over spatial frequency of the full-view data set (left figure) and the off-axis data set (right figure).

Table 1. Quantitative comparison of the data sets by means of parameters of the fitted Gaussians. Using the FWHM of the background signals and the mean values (center positions of the histogram peaks) x_c of the Gaussian peaks of stratum moleculare (A), white matter (B) and stratum granulosum (C) and contrast-to-noise ratios c between the structures were calculated.

	FWHM formalin [$\cdot 10^{-9}$]	$\mathbf{x_c}$ **A** [$\cdot 10^{-9}$]	$\mathbf{x_c}$ **B** [$\cdot 10^{-9}$]	$\mathbf{x_c}$ **C** [$\cdot 10^{-9}$]	**c A-B**	**c B-C**	**c A-C**
conventional reconstruction	1.08	14.98	15.96	19.12	0.91	2.91	3.82
off-axis reconstruction	1.22	14.74	15.94	19.07	0.98	2.57	3.54

dark gray structure corresponds to white matter, the bright gray structure to stratum granulosum and the dark gray outer structure to stratum moleculare. Both stratum granulosum and stratum moleculare are types of gray matter. Beside these three structures it is possible to detect blood vessels, which appear white. The plot at the bottom of Fig. 5 presents a comparison between section profiles through these two slices. Here a slight difference between the line plots can easily be detected. It is noticeable that the positions of the different features within the slices seem to be equal. However, the $\Delta\delta$ values differ up to $2{\cdot}10^{-9}$.

In order to quantify these differences histograms of the 3D data sets were performed, as illustrated in Fig. 6. Using multi Gaussians fits through the histograms the peak positions (x_c) of the structures and the full width at half maxima (FWHM) of the formalin were calculated (see Tab. 1). Using the definition

$$c = \frac{|x_{c1} - x_{c2}|}{\mathrm{FWHM}_{\mathrm{formalin}}} \tag{3}$$

the contrast-to-noise ratios c between the different structures were determined. Using this definition a value $c > 1$ is required in order to distinguish anatomical structures using intensity-based algorithms. A comparison of the contrast-to-noise ratios shows that the values for the full-view reconstruction are very similar to the off-axis values.

3.3 Spatial resolution

Twice the absorption grating period p_2 gives the lowest limit of the spatial resolution which can be achieved using a grating interferometer [15]. For higher Talbot distances this values becomes higher. Furthermore the detection system limits the spatial resolution. In order to compare the spatial resolution between the two differently reconstructed data sets an estimation by means of Fourier analysis of the reconstructed slices was performed. There, the radial spectral power (rSP) of a structure ($\mathrm{rSP}_{\mathrm{struc}}$) within the specimen was determined and divided by the rSP of the background signal ($\mathrm{rSP}_{\mathrm{back}}$) [28]. The ratio R is then plotted against the spatial frequency (cp. Fig. 7). Using a exponential decay fit the baseline of the diagram (R_{base}) can be determined. Finally, the spatial resolution was estimated as the first observed frequency greater than twice the mean value of the baseline R_{base}. For the full-view reconstruction this value was 19.9 line pairs per millimeter (LP mm^{-1}), for the off-axis scan 12.8 LP mm^{-1}. These values correspond to peak to peak distances of around 50 μm for the full-view scan and 78 μm for the off-axis scan. The spatial resolution was taken as half of these values, resulting in 25 μm and 39 μm as given in literature [29].

4. CONCLUSIONS

This study confirms that X-ray phase tomography obtained by a combination of SRμCT with a grating interferometer is a unique tool for imaging human brain tissue with cellular resolution. The specific investigation of half-object data acquisition with the tomography rotation axis positioned off-center (near the edge of the field) undertaken in this study, and its comparison with the full-view case, show that the data treatment procedures - especially the offset correction of the differential phase projections - can be adapted to the off-center case without

noticeable loss in contrast-to-noise ratio of the phase tomograms, though - at least in the case investigated here - at 50% loss in spatial resolution. In summary, the results show that, for tomography of objects wider than the instrument field of view, half-object acquisition with an off-centered rotation axis is just as interesting for grating interferometric phase tomography as it has been proved in the past years to be for absorption-contrast tomography.

ACKNOWLEDGMENTS

The authors gratefully acknowledge P. Zimmermann (University of Basel) for the extraction of the human brain and K. Scheffler and H. Crooijmans (University of Basel) for the MRI measurements of the brain. The project was partially funded by Swiss National Science Foundation (CR23I2_125 406) and was supported by beam time from the ESRF (proposal MD-407). We acknowledge financial support through the DFG Cluster of Excellence Munich-Centre for Advanced Photonics (MAP), the DFG Gottfried Wilhelm Leibniz program and the European Research Council (ERC, FP7, StG 240142). This work was carried out with the support of the Karlsruhe Nano Micro Facility (KNMF, www.kit.edu/knmf), a Helmholtz Research Infrastructure at Karlsruhe Institute of Technology (KIT). One of the authors (T. W.) acknowledges support from the French research networks (RTRA) "Digiteo" and "Triangle de la Physique" (grants 2009-034T and 2009-79D).

REFERENCES

[1] Müller, B., Bernhardt, R., Weitkamp, T., Beckmann, F., Bräuer, R., Schurigt, U., Schrott-Fischer, A., Glueckert, R., Ney, M., Beleites, T., Jolly, C., and Scharnweber, D., "Morphology of bony tissues and implants uncovered by high-resolution tomographic imaging," *Int. J. Mater. Res.* **98**, 613–621 (2008).

[2] Stock, S. R., "Recent advances in X-ray microtomography applied to materials," *Int. Mater. Rev.* **53**, 129–181 (2008).

[3] Kyrieleis, A., Ibison, M., Titarenko, V., and Withers, P. J., "Image stitching strategies for tomographic imaging of large objects at high resolution at synchrotron sources," *Nucl. Instrum. Methods Phys. Res., Sect. A* **607**, 677684 (2009).

[4] Fitzgerald, R., "Phase-sensitive X-ray imaging," *Phys. Today* **53**, 23–26 (2000).

[5] Momose, A., "Recent advances in X-ray phase imaging," *Jpn. J. Appl. Phys.* **44**, 6355–6367 (2005).

[6] Schulz, G., Weitkamp, T., Zanette, I., Pfeiffer, F., Beckmann, F., David, C., Rutishauser, S., Reznikova, E., and Müller, B., "High-resolution tomographic imaging of a human cerebellum: Comparison of absorption and grating based phase contrast," *J. R. Soc. Interface* **7**, 1665–1676 (2010).

[7] Bonse, U. and Hart, M., "An X-ray interferometer," *Appl. Phys. Lett.* **6**, 155–156 (1965).

[8] Momose, A., Takeda, T., Itai, Y., and Hirano, K., "Phase-contrast X-ray computed tomography for observing biological soft tissues," *Nat. Med.* **2**, 473 – 475 (1996).

[9] Snigirev, A. A., Snigireva, I., Kohn, V., Kuznetsov, S., and Schelokov, I., "On the possibilities of x-ray phase contrast microimaging by coherent high-energy synchrotron radiation," *Rev. Sci. Instrum.* **66**, 5486–5492 (1995).

[10] Cloetens, P., Barrett, R., Baruchel, J., Guigay, J.-P., and Schlenker, M., "Phase objects in synchrotron radiation hard x-ray imaging," *J. Phys. D: Appl. Phys.* **29**, 133–146 (1996).

[11] Förster, E., Goetz, K., and Zaumseil, P., "Double crystal diffractometry for the characterization of targets for laser fusion experiments," *Krist. Tech.* **15**, 937–945 (1980).

[12] Davis, T. J., Gao, D., Gureyev, T. E., Stevenson, A. W., and Wilkins, S., "Phase-contrast imaging of weakly absorbing materials using hard X-rays," *Nature* **373**, 595–598 (1995).

[13] David, C., Nöhammer, B., Solak, H. H., and Ziegler, E., "Differential X-ray phase contrast imaging using a shearing interferometer," *Appl. Phys. Lett.* **81**, 3287–3289 (2002).

[14] Momose, A., Kawamoto, S., Koyama, I., Hamaishi, Y., Takai, K., and Suzuki, Y., "Demonstration of X-ray Talbot interferometry," *Jpn. J. Appl. Phys., Part 2* **42**, 866–868 (2003).

[15] Weitkamp, T., Diaz, A., David, C., Pfeiffer, F., Stampanoni, M., Cloetens, P., and Ziegler, E., "X-ray phase imaging with a grating interferometer," *Opt. Express* **13**, 6296–6304 (2005).

[16] Müller, B., Schulz, G., Mehlin, A., Herzen, J., Lang, S., Holme, M., Zanette, I., Hieber, S., Deyhle, H., Beckmann, F., Pfeiffer, F., and Weitkamp, T., "Grating-based tomography of human tissues ," *AIP Conf. Proc.* **1466**, 107–112 (2012).

[17] Pfeiffer, F., David, C., Bunk, O., Poitry-Yamate, C., Grütter, R., Müller, B., and Weitkamp, T., "High-sensitivity phase-contrast tomography of rat brain in phosphate buffered saline," *J. Phys. Conf. Ser.* **186**, 0120461–0120463 (2009).

[18] Pfeiffer, F., Bunk, O., David, C., Bech, M., Le Duc, G., and Bravin, A. Cloetens, P., "High-resolution brain tumor visualization using three-dimensional X-ray phase contrast tomography," *Phys. Med. Biol.* **52**, 6923–6930 (2007).

[19] Pinzer, B. R., Cacquevel, M., Modregger, P., McDonald, S. A., Bensadoun, J. C., Thuering, T., Aebischer, P., and Stampanoni, M., "Imaging brain amyloid deposition using grating-based differential phase contrast tomography," *Neuroimage* **61**, 1336–1346 (2012).

[20] Schulz, G., Morel, A., Imholz, M. S., Deyhle, H., Weitkamp, T., Zanette, I., Pfeiffer, F., David, C., Müller-Gerbl, M., and Müller, B., "Evaluating the microstructure of human brain tissues using synchrotron radiation-based micro computed tomography," *Proc. SPIE* **7804**, 78040F (2010).

[21] Müller, B., Schulz, G., Herzen, J., Mushkolaj, S., Bormann, T., Beckmann, F., and Püschel, K., "Morphology of urethral tissues," *Proc. SPIE* **7804**, 78040D (2010).

[22] Schulz, G., Crooijmans, H. J., Germann, M., Scheffler, K., Müller-Gerbl, M., and Müller, B., "Three-dimensional strain fields in human brain resulting from formalin fixation," *J. Neurosci. Methods* **202**, 17–27 (2011).

[23] Weitkamp, T., Zanette, I., David, C., Baruchel, J., Bernard, P., Bech, M., Deyhle, H., Donath, T., Kenntner, J., Lang, S., Mohr, J., Müller, B., Pfeiffer, F., Reznikova, E., Rutishauser, S., Schulz, G., Tapfer, A., and Valade, J.-P., "Recent developments in X-ray Talbot interferometry at ESRF-ID19," *Proc. SPIE* **7804**, 780406 (2010).

[24] Weitkamp, T., David, C., Kottler, C., Bunk, O., and Pfeiffer, F., "Tomography with grating interferometers at low-brilliance sources," *Proc. SPIE* **6318**, 63180S (2006).

[25] Faris, G. W. and Byer, R. L., "Three-dimensional beam-deflection optical tomography of a supersonic jet," *Appl. Opt.* **27**, 5202–5212 (1988).

[26] Pfeiffer, F., Kottler, C., Bunk, O., and David, C., "Hard X-ray phase tomography with low-brilliance sources," *Phys. Rev. Lett.* **98**, 108105 (2007).

[27] Pfeiffer, F., Bunk, O., Kottler, C., and David, C., "Tomographic reconstruction of three-dimensional objects from hard X-ray differential phase contrast projection images," *Nucl. Instrum. Methods Phys. Res. Sect. A* **580**, 925–928 (2007).

[28] Modregger, P., Lübbert, D., Schäfer, P., and Köhler, R., "Spatial resolution in Bragg-magnified X-ray images as determined by Fourier analysis," *Phys. Status Solidi A* **204**, 27462752 (2007).

[29] Wang, L., Ho, P. P., Liu, C., Zhang, G., and Alfano, R. R., "Ballistic 2-D imaging through scattering walls using an ultrafast optical Kerr gate," *Science* **253**, 769771 (1991).